Effect of Airborne Hydrocarbons on the Wettability of Phase Change Nanoparticle Decorated Surfaces

Guo, Weiteng; Chen, Bin; Do, Van Lam; Ten Brink, Gert H.; Kooi, Bart J.; Svetovoy, Vitaly B.; Palasantzas, George

Published in:
Acs Nano

DOI:
10.1021/acsnano.9b06909

Publication date:
2019

ACS NANO

Cite This: ACS Nano 2019, 13, 13430−13438

www.acsnano.org

ARTICLE

Effect of Airborne Hydrocarbons on the Wettability of Phase Change Nanoparticle Decorated Surfaces

Weiteng Guo,[†] Bin Chen,[†] Van Lam Do,[†] Gert H. ten Brink,[†] Bart J. Kooi,[†] Vitaly B. Svetovoy,[†,‡] and George Palasantzas*[,†]

[†]Zernike Institute for Advanced Materials, University of Groningen, Nijenborgh 4, 9747 AG Groningen, The Netherlands

[‡]A. N. Frumkin Institute of Physical Chemistry and Electrochemistry, Russian Academy of Sciencies, Leninsky prospect 31 bld. 4, 119071 Moscow, Russia

Supporting Information

ABSTRACT: We present here a detailed study of the wettability of surfaces nanostructured with amorphous and crystalline nanoparticles (NPs) derived from the phase-change material $Ge_2Sb_2Te_5$ (GST). Particular attention was devoted to the effect of airborne surface hydrocarbons on surface wetting. Our analysis illustrates that a reversible hydrophilic−hydrophobic wettability switch is revealed by combined ultraviolet-ozone (UV-O_3) treatments and exposure to hydrocarbon atmospheres. Indeed, the as-prepared surfaces exhibited a hydrophilic state after thermal annealing or UV-O_3 treatment which can partially remove hydrocarbon contaminants, while a hydrophobic state was realized after exposure to hydrocarbon atmosphere. Using high-angle annular dark-field scanning transmission electron microscopy for the specially designed GST NP decorated graphene substrates, a network of hydrocarbon connecting GST NPs was observed. Our findings indicate that airborne hydrocarbons can significantly enhance the hydrophobicity of nanostructured surfaces. Finally, the experiments reveal that previously defined hydrophilic materials can be used for the design of hydrophobic surfaces even if the meniscus is highly adhered to a solid surface, which is in agreement with our qualitative model involving the contribution of the nanomeniscus formed between the substrate and a decorating NP.

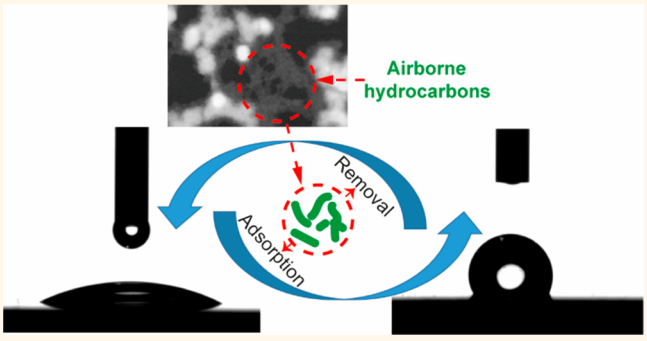

KEYWORDS: *wetting, airborne hydrocarbons, $Ge_2Sb_2Te_5$, nanoparticle, wettability switch, transmission electron microscopy, nanomeniscus*

Nowadays relentless efforts have been devoted to creating different types of roughness in order to control the wettability of surfaces, including mimicking of natural structures to generate the well-known "lotus"[1−3] and "rose petal"[4] effects. The drive is to meet various demands for technology applications or realize certain functions such as self-cleaning,[5] anti-icing,[6] heat exchangers,[7] and fog harvesters.[8] Processes to form hydrophobic surfaces involve combinations of surface roughening with the alteration of surface chemistry using low surface energy materials to mimic for example the structure of the lotus leaf or butterfly wings that show strong hydrophobicity.

In general, the surface wettability is characterized by the static contact angle (SCA) as well as by the dynamic contact angles termed as advancing and receding contact angles (ACA/RCA) between a testing water droplet and a surface. The SCA of a testing droplet on a flat surface can be described by the Young's equation[9] $\gamma_{sv} = \gamma_{sl} + \gamma_{lv}\cos\theta_Y$, where γ_{sv}, γ_{sl}, and γ_{lv} are the surface energies of solid−air, solid−liquid, and liquid−air, respectively, and θ_Y represents the SCA of the liquid on the flat solid surface. When $\gamma_{sv} - \gamma_{sl} < 0$, one obtains $\theta_Y > 90°$ and the surface is termed as hydrophobic, while when $\gamma_{sv} - \gamma_{sl} > 0$, one obtains $\theta_Y < 90°$ and the surface is termed as hydrophilic. However, for rough surfaces, Wenzel[10] and Cassie−Baxter[11] models have been widely used to describe the effect of roughness on surface wettability. In Wenzel theory (see Figure 1a), the testing droplet wets the surface cavities leading to increased interaction area with the liquid droplet. In terms of Wenzel model the apparent SCA θ_W is given by the expression[10] $\cos\theta_W = r\cos\theta_Y$, where r is the roughness factor.

Received: August 30, 2019
Accepted: October 18, 2019
Published: October 18, 2019

DOI: 10.1021/acsnano.9b06909
ACS Nano 2019, 13, 13430−13438

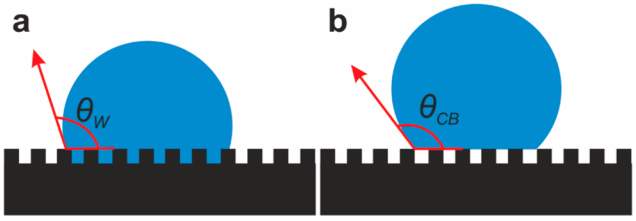

Figure 1. Schematics of the two models that describe the relationship between wettability and roughness. (a) Wenzel model, and (b) Cassie–Baxter model.

The latter is given by $r = A_r/A_p$ where A_r is the actual rough surface area, and A_p is the projected surface area on the average surface plane. Since $r > 1$, the absolute value of cos θ_W is increased, indicating consistency in wettability so that the hydrophilic/hydrophobic surfaces would become more hydrophilic/hydrophobic with increasing surface roughness. However, in several cases, for example, the lotus effect,[1−3] the droplet will not wet fully the surface, leaving air pockets within surface cavities (see Figure 1b). This case is described as Cassie–Baxter model, where the apparent SCA θ_{CB} is given by the expression[11] cos $\theta_{CB} = f$cos $\theta_y + (f - 1)$, where f is the fraction of the solid surface area wetted by the liquid. This model does not preserve consistency of wettability as in Wenzel state, since a hydrophobic surface can be obtained also from a hydrophilic one.

Nevertheless, several other studies[12−14] have demonstrated complex cases of surface wettability, where Wenzel and Cassie–Baxter models could not explain the experimental data. Using the concept "work of adhesion" that was introduced by Dupré,[15] and taking the air–liquid interface on a solid as a one-dimensional system, Pease[12] emphasized that the SCA is the result of an equilibrium position that the three-phase contact line (TPL) could reach. Then the dynamic contact angles RCA and ACA were also expressed in terms of the work of adhesion.[14,16] Through experiments on nanofibrous membranes, Wang[17] argued that the 90° could not be used as the mathematical wetting threshold between the hydrophobicity and hydrophilicity in designing nanofibrous surfaces. Derjaguin[18,19] discovered the solid surface is prewetted by a wetting film when in contact with a liquid droplet and described the film with the concept of the disjoining pressure.

Furthermore, airborne hydrocarbon contaminants, for example, alkanes, alkenes, aromatics, and alcohols can be easily adsorbed by various types of surfaces including gold,[20] graphene,[21] TiO_2,[22] boron nitride nanotube decorated surfaces,[23] and Ni–Cu–P ternary coating.[24] By comparison of the results of wetting measurement and Fourier transformed infrared (FTIR) spectroscopy of surfaces before and after ultraviolet-ozone (UV-O_3) treatments, which is an effective method for removing surface organic contaminants,[25] Li *et al.*[21] proved that the wettability variation of graphene was the result of adsorption/removal of airborne hydrocarbons. They attributed the effect of airborne hydrocarbons on the graphene wettability to be the result of reduced surface energy. Although the FTIR results could provide direct evidence of the adsorption–removal of airborne hydrocarbon contaminants, the distribution as well as the morphology of these surface contaminants, which is very important to reveal their effect on surface wettability, are still unclear. Therefore, more detailed characterization is necessary to evaluate the specific effect of airborne hydrocarbons on the enhancement of hydrophobicity of various surfaces, especially for micro/nanostructured surfaces.

In this framework, nanoparticles (NPs) provide an ideal decoration method able to create nanostructured surfaces and achieve certain wettability, for example, TiO_2 NP painting,[26] or even more directly, for example, Cu NP deposition by a high-pressure magnetron sputtering system where the production and decoration process can be accomplished in one step.[27] In addition, NPs derived from the phase-change material (PCM) $Ge_2Sb_2Te_5$ (GST), which has been used as an active medium in rewritable optical disks, that is, CD, DVD, and blu-ray disks,[28,29] offer more extensive possibilities to study wetting on nanostructured surfaces than other material systems. This is because the surface energy of PCMs can be altered by the amorphous to crystalline phase transformation without significant alteration of its composition and morphology, providing another degree of freedom to tailor the surface wettability.

Therefore, we used here GST NPs both in their amorphous and crystalline phases as a means of nanostructuring in order to study in depth the intrinsic relationship of the wettability of nanostructured surfaces and airborne hydrocarbons. Moreover, graphene, which has found promising applications in sequencing,[30] energy storage,[31] filtration,[32] and surface coating,[33] offers superior mechanical properties[34] that allowed the designing of GST NPs/graphene samples to observe the distribution as well as the morphology of airborne hydrocarbons on nanostructured surfaces by high-angle annular dark-field scanning transmission electron microscopy (HAADF-STEM). Hence, the effect of hydrocarbon adsorption on the wettability of GST NP decorated surfaces was extensively investigated *via* a wettability switch between hydrophilic–hydrophobic states due to the removal/adsorption of hydrocarbons by UV-O_3 treatments/hydrocarbon exposure. Subsequently, the experimental results were theoretically explained by introducing the contribution of the nanoscale meniscus between the substrate and a NP to the wettability of NP decorated surfaces.

RESULTS AND DISCUSSION

Wettability of Flat Substrate Surfaces Prior to NP Deposition. The evolution of the wettability of the bare Cu substrate surface with time is shown in Figure 2a. The bare Cu substrates (for bare Cu surface wetting measurement as well as GST NPs deposition which will be discussed later) were made from mechanically polished polycrystalline Cu blocks with purity of 99.99%. Then the Cu substrates were ultrasonically cleaned with acetone, ethanol, and water, respectively, where each step of ultrasonic cleaning lasted at least 30 min. After UV-O_3 treatment, the SCA of the Cu surface is 34 ± 1°, while after further exposure to air, the SCA rose to 64 ± 1° within 1 day and finally after 3 days was saturated at 79.5 ± 1.5° without any significant change for the next 3 weeks (79 ± 1°). Similarly, the wettability of amorphous and crystalline GST films is shown in Figure 2b. Indeed, both the amorphous and crystalline GST thin films show superhydrophilicity (SCA~0°) after 20 min UV-O_3 treatment. Then the SCA of the two surfaces increased to 48° and 27.5 ± 0.5°, respectively, and stabilized to the values of 48.5 ± 0.5° and 31 ± 1° within a week (Figure 2).

For convenience, the SCAs of the surfaces in Figure 2 are redefined as follows: (i) the SCAs of the freshly UV-O_3 treated

DOI: 10.1021/acsnano.9b06909
ACS Nano 2019, 13, 13430−13438

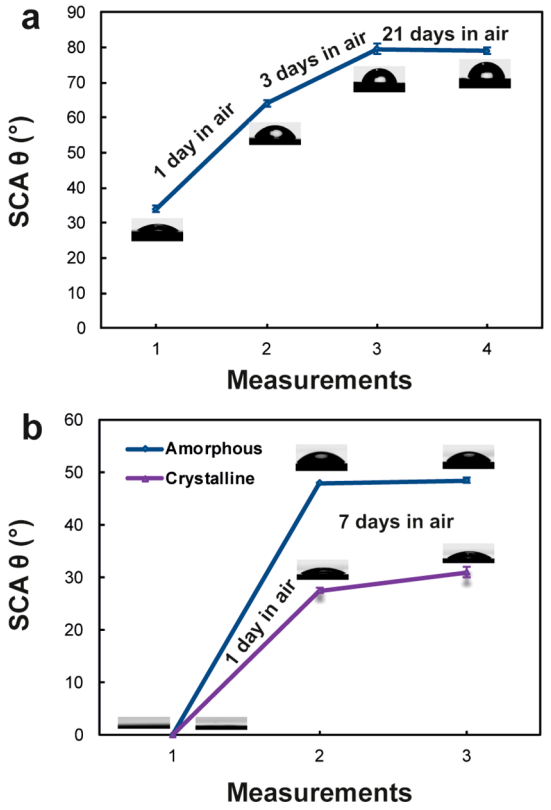

Figure 2. Wettability measurements on relatively flat surfaces of the substrate materials used for decoration with GST NPs. (a) Evolution of SCA of the bare Cu substrate surface. (b) Evolution of SCA on amorphous and crystalline deposited GST thin films.

surface are defined as θ^{U} (θ^{U}_{Cu},θ^{U}_{Amo}, and θ^{U}_{Cry} for bare Cu, amorphous GST, and crystalline GST film, respectively), and (ii) the SCAs after long-time exposure in air, where the surfaces can adsorb hydrocarbons, are defined as θ^{H} (θ^{H}_{Cu}, θ^{H}_{Amo}, and θ^{H}_{Cry} for bare Cu, amorphous GST, and crystalline GST films, respectively). The wettability of the involved surfaces from Figure 2 is summarized in Table 1.

Table 1. θ^{U} and θ^{H} of the flat surfaces made of Cu, amorphous GST, and crystalline GST[a]

materials	θ^{U} (deg)	θ^{H} (deg)
substrate Cu	34	79
amorphous GST	0	48.5
crystalline GST	0	31

[a] θ^{U}: Contact angle of the flat surface with the relevant material measured immediately after UV-O_3 treatment. θ^{H}: Contact angle of the flat surface with the relevant material measured after long-time exposure in air.

Wettability Variation in Air After Thermal Annealing and UV-O_3 Treatments. A GST NP decorated Cu surface was fabricated using high-pressure magnetron sputtering,[35] having high coverage of NPs (ratio of area covered NPs with respect to the overall area determined by TEM images) of ~95% as it is shown in Figure 3a. The selected area electron diffraction (SAED) pattern, (inset of Figure 3a) shows that the GST NPs are in the amorphous state. CA measurements were conducted afterward, and the results are shown in Figure 3b. The SCA of the as-prepared sample was 88.5 ± 0.5° and then

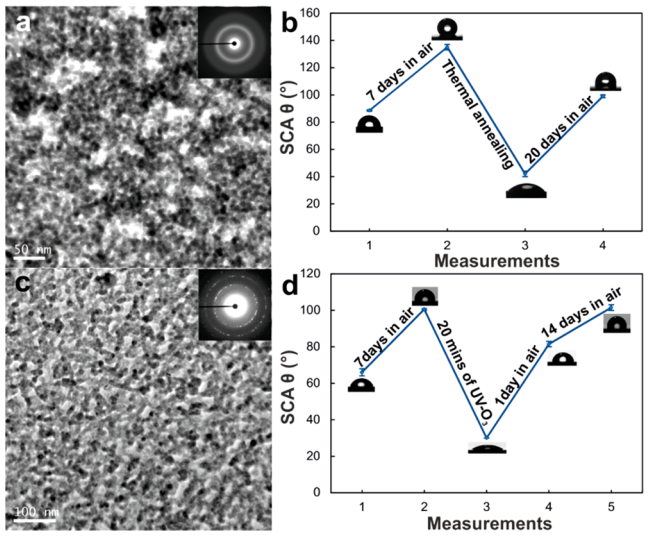

Figure 3. Experimental data of GST NPs on Cu substrates. (a) TEM image of amorphous GST NPs deposited on a TEM grid simultaneously with the NPs deposited on the Cu substrate. (b) Evolution of the SCA of the as-deposited amorphous GST NPs on a Cu substrate with subsequent thermal annealing at 180 °C. (c) TEM image of as-deposited crystalline GST NPs on a TEM grid. (d) Evolution of the SCA for the as-deposited crystalline NPs on a Cu substrate after several UV-O_3 treatments and subsequent exposures to air.

rose to 135 ± 2° after storing the sample in air for 7 days. Subsequently, the sample was annealed at 180 °C for 5 min in a quartz tube with base pressure in the ultrahigh-vacuum range (~10^{-9} mbar) and then was cooled down to room temperature. The CA measurements were conducted immediately after the thermal annealing process, and the low SCA value (42 ± 2°) indicates an annealing-induced hydrophobic–hydrophilic transition. Then the SCA of the sample increased to 99 ± 1° after keeping it in air for 4 days, indicating a hydrophilic–hydrophobic transition. After 20 days, the SCA slightly increased to ~101.5 ± 1.5°. The annealing temperature 180 °C is higher than the crystallization temperature (T_c) of GST NPs (the T_c of the as-prepared GST NPs was deduced to be 148 C° to 150 C° in our previous work),[35] and the annealing time (5 min) is sufficiently long to ensure full crystallization of the GST NPs.[35] Thermal annealing has been reported to lower the SCA of surfaces because adsorbed hydrocarbons can be partly removed by this process,[21] yielding hydrophobic–hydrophilic transitions. Nevertheless, the SCA of the sample could not recover back to the initial hydrophobic (135 ± 2°) state after nearly 1 month storage in air. We attributed this change in SCA to the changes of the surface topography as well as the surface energy of the GST NPs after crystallization by thermal annealing,[36] as it will be discussed later on.

Furthermore, we evaluated the wettability of Cu surfaces decorated with the as-deposited crystalline GST NPs. Indeed, the SAED pattern (inset of Figure 3c) shows an identical structure as in our previous studies,[35] confirming the crystalline nature of the GST NPs. The coverage of the GST NPs was ~96%, which is similar to that of the amorphous GST NPs sample used for thermal annealing in Figure 3a. The evolution of SCA shows similar behavior as the amorphous one, as shown in Figure 3d. The SCA of the as-prepared sample with crystalline GST NPs was 66 ± 2° and increased to 105 ± 0.5° after the sample was kept in air for 7 days. The SCA

DOI: 10.1021/acsnano.9b06909
ACS Nano 2019, 13, 13430–13438

immediately dropped down to 30° after 20 min of UV-O_3 treatment. After 1 day of storage in air, the SCA of the sample rose to 81.5 ± 1.5°, remained at the same value for another day, and then increased to 100.5 ± 0.5° within an additional day. Finally, the SCA was measured to be 101.5 ± 1.5° after 2 weeks, showing agreement with the results of the annealed sample (Figure 3b). For consistency, the as-prepared crystalline GST NPs sample underwent another 20 min UV-O_3 treatment, and the SCA decreased again to around 30°. Given the fact that the adsorbed hydrocarbons can be partially removed by thermal annealing or UV-O_3 treatment, it is evident that airborne hydrocarbons play an important role in the wettability of NP decorated surfaces. Hence, in order to investigate further the effect of airborne hydrocarbons on the wettability of NP decorated surfaces, an atmosphere with a higher concentration and better control of hydrocarbons was created to compare to the effects triggered by exposure to ambient air.

Wettability Switch in Designed Hydrocarbon Atmosphere and UV-O_3 Treatment. Two specimens based on Cu surfaces decorated with amorphous GST NPs, labeled as sample 1 (S1) and sample 2 (S2), were made using the high-pressure magnetron sputtering system.[35] The CA measurements in Figure 4a were conducted for both samples immediately after the GST NPs deposition. Then the measurements were taken every 24 h (or immediately after each UV-O_3 treatment) to check the temporal evolution of the wettability of the samples. The SCAs of S1 and S2 were ~63 ± 4° and ~59 ± 3°, respectively (marked as "Measurement 1" in Figure 4a). After being kept in ambient air for 7 days, the SCAs of both samples increased to around ~120° (marked as "Measurement 2" in Figure 4a). After 20 min of UV-O_3 treatment using a UV-O_3 sterilizer (labeled with NZX Sahne portable), the CA of both samples dramatically drops to around 25° (marked as "Measurement 3" in Figure 4a), showing an obvious hydrophobic−hydrophilic transition. Aiming to extensively evaluate the effect of hydrocarbons adsorbed by the NP decorated surfaces, more CA measurements were conducted subsequently on S1 and S2. Indeed, S1 was kept in ambient air, while S2 was kept in the hydrocarbon atmosphere (H-A) that was created in a Petri dish by using octane (see Figure S1). After 1 day, the SCA of S1 increased to 91.5 ± 1.5°, while the SCA of S2 increased to 119 ± 1° (marked as "Measurement 4" in Figure 4a). Both samples experienced a hydrophilic−hydrophobic transition, and the SCA rose faster when the samples were exposed to a hydrocarbon atmosphere.

In order to crosscheck the previous result and exclude the difference in SCA concerning the individual difference between S1 and S2, the storage conditions of the two samples were exchanged after a second UV-O_3 treatment. The SCA of the two samples decreased back to around ~25° after the second UV-O_3 treatment (see "Measurement 5" in Figure 4a), which is identical with the "Measurement 3" in Figure 4a. Then the sample S1 and S2 were kept in hydrocarbon atmosphere and ambient air separately. After 1 day, the hydrophilic−hydrophobic transition appeared again for both samples, where the SCA of S1 and S2 rose to 117 ± 1° and 98 ± 2°, respectively (see "Measurement 6" in Figure 4a). The latter shows consistency with the results of "Measurement 4" and excluded the individual difference factor between the two samples. Subsequently, the two samples were kept in their original conditions for 3 days (*i.e.*, S1 in H-A and S2 in air) where the

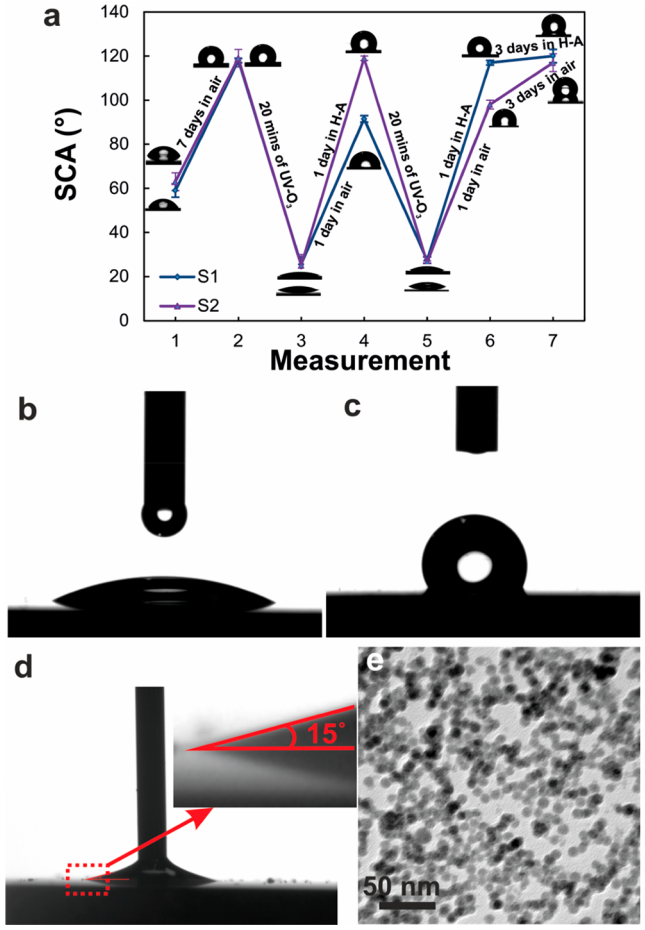

Figure 4. Characterization of amorphous GST NP decorated samples. (a) Variation of SCA of two amorphous GST NP decorated Cu samples after UV-O_3 treatments. (b) SCA of the amorphous GST NP decorated Cu sample after UV-O_3 treatment. (c) SCA of the amorphous GST NP decorated Cu sample after being kept in ambient air. (d) Receding contact angle of an amorphous GST NP decorated Cu sample after being kept in ambient air. (e) TEM image of NPs deposited on a TEM grid simultaneously with the NPs that decorated the Cu samples. The coverage of the amorphous was 72%, and the diameter of the NPs was 9.8 ± 0.5 nm.

SCA of S1 saturated to values 120 ± 3°, while the SCA of S2 steadily climbed to 117 ± 4°. Comparing the storage conditions of ambient air and H-A, the main difference lies in the concentration of hydrocarbons, and the results in Figure 4a indicate that higher airborne hydrocarbon concentration could boost the process of transforming the hydrophilic to the hydrophobic state for the as-prepared samples after UV-O_3-induced removal of adsorbed hydrocarbons. Therefore, it is reasonable to expect that the hydrocarbons adsorbed by the surfaces play an important role in the hydrophilic−hydrophobic transition of GST NP decorated Cu.

Additionally, the wetting state of the two samples immediately after UV-O_3 treatment is termed as a "hydrophilic state" with a typical image as in Figure 4b, while the wettability of the samples after 1 day storage in H-A or 4 days storage in ambient air, which show strong hydrophobicity (SCA > 100°), is termed as a "hydrophobic state" with a typical image as in Figure 4c. Moreover, the ACA was measured to be 123° (see Movie 1 in Supporting Information), while the RCA was

DOI: 10.1021/acsnano.9b06909
ACS Nano 2019, 13, 13430−13438

measured to be 15° (see Figure 4d). The RCA was indicated directly on the image instead of using the fitting model based on the ellipse outline. This is because the sectional view of the outline of the testing droplet tends to show a triangular shape due to the strong adhesion force between the surface and the testing droplet. Subsequently, the hysteresis (θ_H) of the as-prepared sample, which is defined as the difference between ACA (θ_A) and RCA (θ_R) with $\theta_H = \theta_A - \theta_R$,[37] was calculated to be 108°.

Characterization of Hydrocarbons on GST NP Decorated Surfaces. In order to understand the effect of hydrocarbons adsorbed on NP decorated surfaces, we performed HAADF-STEM imaging measurements to gain insight on the distribution and morphology of adsorbed hydrocarbons. Because the contrast in HAADF-STEM is related to the thickness and the square of average atomic number of the corresponding atomic column, the thin thickness and low average atomic number of adsorbed hydrocarbons will yield weak contrast for the adsorbed hydrocarbons that will be obscured by the substrate material. Therefore, not only the average atomic number but also the thickness of the substrate should be low enough to minimize the contrast interference during HAADF-STEM measurements. Monolayer graphene, having a low atomic number (6 C) and being extremely thin (1 atomic layer thick), is a perfect candidate satisfying the stringent criteria of this particular sample design to observe the adsorption of surface hydrocarbons. Moreover, the superior mechanical properties (elastic modulus and intrinsic breaking strength) of graphene[34] renders this system as a promising candidate to support decoration with GST NPs by the magnetron sputtering deposition. Hence, a monolayer (partly bilayer or trilayer) graphene was synthesized by chemical vapor deposition (CVD), and subsequently, the graphene layer was transferred onto a Quantifoil R2/1 holey carbon (Electron Microscopy Sciences, Q225-AR1) TEM grid, which served as the substrate for NPs deposition in the magnetron sputtering system. Finally, the sample was kept in ambient air for 3 weeks to adsorb sufficient coverage of hydrocarbons for later TEM observations.

The morphology of GST NPs/graphene sample is shown in Figure 5a. The dark circles are GST NPs, and there is an obvious difference in the contrast with the background. The left bottom part of Figure 5a, divided by the red dashed line, refers to graphene/carbon support, while the top right part, where the contrast is relatively brighter, is mostly the suspended monolayer graphene shown in Figure 5b. The bright areas with spherical like features in Figure 5c (with high contrast) are the GST NPs, while the dark areas (with low contrast) are supposed to be the graphene. However, there are also some "conjunctions" among the NPs showing a "cloudy" contrast (obviously distinct in between the bright and dark parts), which are presumably the adsorbed airborne hydrocarbons. Figure 5d is the bright-field (BF) STEM image, which in line with Figure 5c also shows the outline of the GST NPs. However, the "cloudy" areas are not visible in Figure 5d, proving that the "cloudy" areas among the NPs in Figure 5c do not present some "heavy" atoms from the materials during sample preparation. Therefore, together with Figure 5c, the BF STEM image also implies that the "cloudy" areas belong to airborne hydrocarbons. The "cloudy" areas are also shown in Figure 5e, where the energy-dispersive X-ray spectroscopy (EDX) mapping data in Figure 5f–h show the material contrasts of the GST NPs. This material outlines overlap with

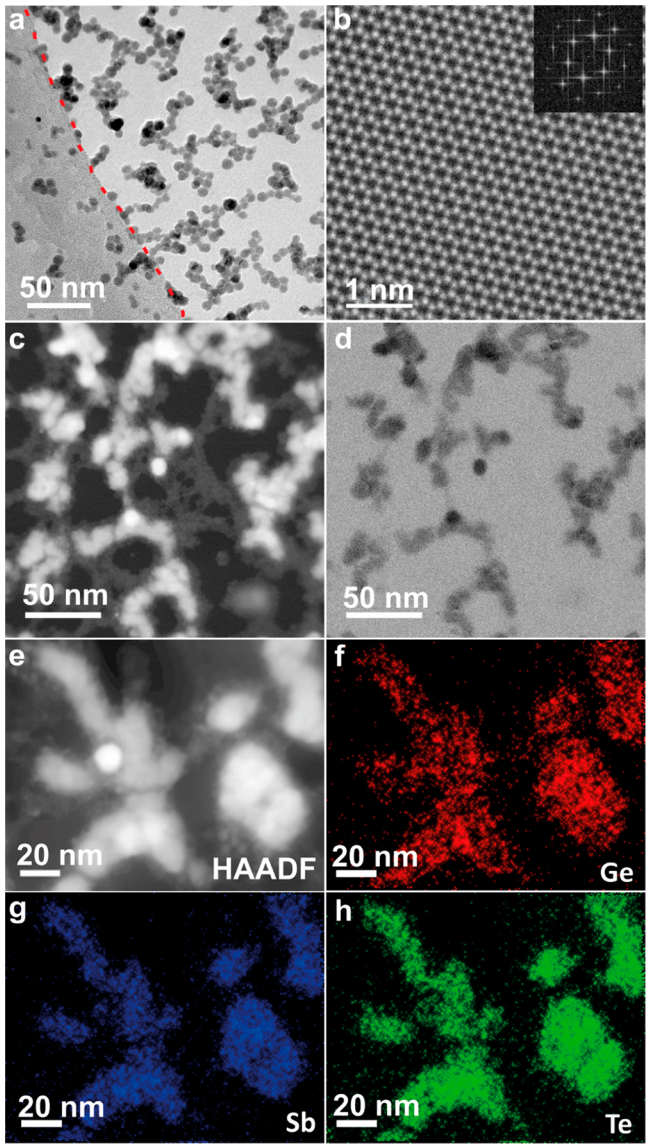

Figure 5. TEM measurements of a GST NPs/graphene sample. (a) BF TEM image of the GST NPs/graphene sample. (b) HAADF-STEM image of the graphene sample with the fast Fourier transform image at the top right corner. (c) HAADF-STEM image of the sample. (d) BF STEM image of the sample taken from the same area of (c). (e) HAADF-STEM image of another area of the same sample. (f–h) EDX mapping of the GST elements Ge, Sb, and Te, respectively.

that of the bright areas in Figure 5e, showing that the Ge/Sb/Te elements mainly locate at this bright area, reconfirming that the "cloudy area" is the hydrocarbon contamination. The results of Figure 5 prove that there are airborne hydrocarbons on the surface of the as-prepared samples after exposure to ambient conditions. The width of the adsorbed hydrocarbons assemblies was measured to be ~7–20 nm in Figure 5c, in equivalent scale with the size of the deposited GST NPs. Moreover, the adsorbed hydrocarbons not only cover the GST NPs but also the intervals of individual NPs on the corresponding substrates.

Effect on Wettability Due to Airborne Hydrocarbons. Here we will attempt to analyze the wettability of the hydrophobic-state of samples decorated by GST NPs where the influence of surface hydrocarbons is the most pronounced.

DOI: 10.1021/acsnano.9b06909
ACS Nano 2019, 13, 13430–13438

Considering the large hysteresis, which implies high adhesion force, Wenzel model[10] comes naturally into consideration. At a first glimpse, this model appears unsuitable for the GST NP decorated surfaces, because it has been applied to mono-component systems instead of a surface decorated with different materials. Considering the substrate and the decorating NPs are materials that can be completely wetted by the testing droplet, the Wenzel model can be modified for describing the binary component system in the form:

$$\cos\theta'_W = f_S\cos\theta_S + f_N\cos\theta_N,$$
$$f_S + f_N = r \quad (1)$$

where θ'_W is the apparent SCA of a binary composite surface in Wenzel state, and θ_S and θ_N are the SCAs for the substrate exposed surfaces and NPs, respectively. Here r ($\geq$1) is the roughness factor with the same definition as indicated before, while f_S and f_N are the ratios of the actual surface area of the exposed substrate and NP surfaces to the projected surface area on a plane that is parallel with the substrate, respectively. Therefore, if the surfaces of the substrate and NPs are both hydrophilic, the binary composite surface would preserve its hydrophilicity, and *vice versa* if both materials are hydrophobic the NP decorated surfaces will be hydrophobic.

The wettability of as-prepared amorphous GST NP decorated Cu surfaces with sufficient coverage C_G (~72%) was analyzed by the modified model of eq 1. Indeed, from Figure 4a, the SCA of the freshly UV-O_3 treated sample was measured to be $\theta^U_{Amo/Cu} = 25°$, while the SCAs of the involved materials (in planar form, see Table 1) were measured immediately after UV-O_3 treatment to be $\theta^U_{Cu} = 34°$ and $\theta^U_{Amo} = 0°$. Assuming that the contacts between GST NPs and the Cu substrate are point-like contacts, we can set for the contact area of the testing water on the Cu substrate $f_S \approx 1$. Because most of amorphous GST NPs are spherical, the factor f_N can be roughly calculated by $f_N \approx 4\pi r_N{}^2 C_G/\pi r_N{}^2 \approx 4C_G$, where r_N is the radius of the NPs. Substituting these parameters in eq 1, we obtain for the theoretical SCA for the freshly UV-O_3 treated sample $\cos\theta^{UT}_{Amo/Cu} > 1$, indicating a superhydrophilic state or $\theta^{UT}_{Amo/Cu} = 0°$. The difference between the calculated and experimental SCAs may stem from the two following reasons: (i) The liquid–solid contact area used in the calculation may differ from the real one (which will be discussed latter and schematically shown in Figure 6), which lead to over estimation of f_S and f_N, giving a lower theoretical SCA. (ii) It is more difficult for adsorbed hydrocarbons to be removed by UV-O_3 treatment on GST NPs than on flat GST surfaces, because the NPs form a porous network with higher content of residual hydrocarbons than the flat GST surface. The latter leads subsequently to stronger surface hydrophobicity. Nevertheless, the experimental value $\theta^U_{Amo/Cu}$ is still lower than θ^U_{Cu}, indicating that the surface roughness due to the deposited NPs can make the original substrate more hydrophilic. Therefore, eq 1 can explain qualitatively the experimental results for the fresh UV-O_3 treated surfaces.

Furthermore, the experimental results from hydrocarbon adsorbed surfaces were also analyzed in terms of eq 1. Substituting the experimental values $\theta^H_{Cu} = 79°$ and $\theta^H_{Amo} = 48.5°$ as well as f_S and f_N (with the same values as the previous calculation after a fresh UV-O_3 treatment yielding $f_S \approx 1$, $f_N \approx 4C_G$) into eq 1, the calculated value of the theoretical SCA for the amorphous GST NP decorated surface yield again $\cos\theta^{HT}_{Amo/Cu} > 1$, indicating a superhydrophilic state with $\cos\theta^{HT}_{Amo/Cu} = 0°$. However, this value is much lower than that of the SCA for the Cu substrate surface ($\theta^H_{Cu} = 79°$), and it has an obvious difference from the experimental value $\theta^H_{Amo/Cu} = 120°$. Obviously, the modified model fails to offer even a qualitative explanation for the wetting state of the amorphous GST NP decorated surface with hydrocarbons adsorbed. In addition, the as-prepared GST NP decorated surface was not in the Cassie–Baxter state, at least in the outer area of the water droplet, because the measured high hysteresis ($\theta_H = 108°$) indicates high adhesion force between the water meniscus and the tested surface. The latter does not occur for the Cassie–Baxter wetting state. Therefore, besides lowering the surface energy, the interaction with porous geometry should be taken carefully into account when evaluating the effect of airborne hydrocarbons on NP decorated surfaces.

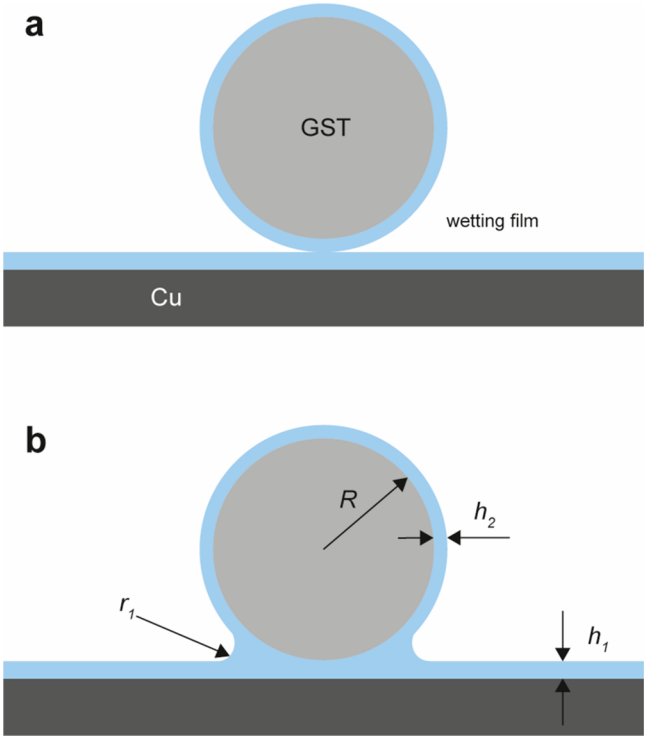

Figure 6. (a) The configuration used to calculate contact angle with eq 1. (b) More realistic geometry of the problem: r_1 is the negative radius of curvature, r_2 (not shown) is the positive radius of curvature in the orthogonal direction to the plane, h_1 is the thickness of wetting film on the substrate, and h_2 is the thickness of wetting film on the NPs.

Amorphous and crystalline GST NP decorated surfaces are found to have a wettability that can be switched by UV-O_3 treatments and hydrocarbon atmospheres. The microstructure and distribution of hydrocarbons adsorbed by amorphous GST NPs decorating surfaces were measured to aid understanding of the effect of airborne hydrocarbons on the wettability of NP decorated surfaces. The evolution of SCAs of the flat surfaces, before and after airborne hydrocarbon adsorption (Table 1), shows that for Cu they change from 34° to 79°, for amorphous GST from ~0° to 48.5°, and for crystalline GST from ~0° to 31°. These results show agreement with previous studies in airborne hydrocarbon tunable wettability of flat surfaces where the SCAs of gold[20] and graphene[21] rose from 0° and 44° to 60° and 80° after adsorption of airborne hydrocarbons,

DOI: 10.1021/acsnano.9b06909
ACS Nano 2019, 13, 13430–13438

respectively. Compared with the wettability evolution of flat surfaces, the SCAs of GST NPs decorating Cu surfaces display a more significant increase in SCAs after airborne hydrocarbon adsorption, where the SCA rose from 25° to 120° (with NP coverage of 72%). However, the significant increase of SCA of the NP decorated surfaces could not be explained by the Wenzel model, which is frequently used for describing the wettability of microstructured surfaces with high wetting hysteresis. Therefore, more efforts should be paid for analyzing our experimental results.

Beyond Wenzel Model. Long ago it was realized[18,38] that the wetting phenomenon is driven by long-range surface forces. For a wetting film of thickness h, the disjoining pressure $\Pi(h)$ was introduced in 1936 by Derjaguin[15,16] (as the difference between the pressures in a region of a phase adjacent to a surface confining this phase and the pressure in the bulk of this phase) to describe the effect of surface interactions. The disjoining pressure is related to the contact angle θ by the equation[18,19]

$$\cos\theta = 1 + \frac{1}{\gamma}\int_{h_0}^{\infty} dh\Pi(h) + \frac{h_0}{\gamma}\Pi(h_0) \tag{2}$$

where $\gamma = \gamma_{lv}$ is the surface tension of liquid, and h_0 is the precursor film thickness ahead of the liquid droplet. In equilibrium, the film thickness is determined from the relation $\Pi(h_0) = P_c$, where P_c is the capillary pressure in the bulk liquid. For macroscopic liquid volumes the capillary pressure $|P_c| \sim \gamma/\mathcal{R}$ is small, where $\mathcal{R}$ is a macroscopic curvature radius of the meniscus. In this case, the last term in eq 2 is small $h_0/\mathcal{R} \ll 1$ since h_0 is in the nanometer range. For this reason, eq 2 is often presented without the last term.[39] Furthermore, the wettability of a material is defined by the integral $I_\Pi = \gamma^{-1}\int_{h_0}^{\infty} dh\Pi(h)$. For $I_\Pi > 0$, the material is superhydrophilic, for $-1 < I_\Pi < 0$, the material is hydrophilic, for $-2 < I_\Pi < -1$, the material is hydrophobic, and for $I_\Pi < -2$, the material is in a nonwetting state. For the case of partial wetting, the typical behavior of the disjoining pressure is shown in Figure S2.

Both materials of interest (Cu and GST) stay hydrophilic (see the results in Table 1) even after exposure to hydrocarbons, and according to eq 1 we cannot obtain the observed hydrophobicity for any parameters of f_S and f_N. Therefore, it is obvious that some important element is missing in the previous analysis. First, let us note that NPs have a small radius of curvature, namely, $R \approx 5$ nm, while eq 2 was derived for flat surfaces. Generalization for the case of curved surfaces has been analyzed in the work by Boinovich and Emelyanenko.[40] Using the general thermodynamic approach, it was found that for a spherical surface, eq 2 is modified in the form:

$$\cos\theta = 1 + \frac{1}{\gamma}\int_{h_0}^{\infty} dh\Pi(h)\left(1 + \frac{h}{R}\right)^2 \tag{3}$$

Here it is assumed that the surface is convex and described by the radius of curvature R, while for a concave surface one has to change $R \to -R$. A significant effect of the curvature is possible only for R comparable with the distance range of the surface forces $h \sim 1$ nm. The modification due to surface curvature is, however, not sufficient to explain the observations since the factor $(1 + h/R)^2$ influences rather the repulsive long-distance tail of the disjoining pressure.

Calculations with eq 1 have been performed for the configuration shown schematically in Figure 6a, while the actual geometry has to look like that shown in Figure 6b. The most important difference is the presence of a concave meniscus with a nanoscopic radius r_1. In the orthogonal direction, the meniscus is convex but with a significantly larger radius $r_2 > r_1$.

Eq 3 does not take the nanomeniscus into account, but it can be included following the same line of reasoning as that used in previous work[40] to deduce eq 3. The disjoining pressure appears in eq 3 as the difference between the pressure in the film P_f and the pressure P_b in the bulk. If there is no meniscus, this difference is equal to the disjoining pressure: $P_f(h) - P_b = \Pi(h)$. The meniscus will contribute to P_f, and in this case one obtains

$$P_f - P_b = -\gamma\left(\frac{1}{r_1} - \frac{1}{r_2}\right) + \Pi(h) \tag{4}$$

The radii of curvature are also functions of the film thickness, but the determination of this dependence is out of the scope of this paper. Our purpose here is to give a qualitative description of the effect. Nevertheless, it is important to mention that $r_2 > r_1$, while R is, in general, the largest in length parameter. Both radii become comparable when $r_1 \sim R$. For $h \ll R$ one can expect that $r_1 \sim h$ with r_1 increasing with h. After substitution, the contact angle θ_N is given by

$$\cos\theta_N = 1 + \frac{1}{\gamma}\int_{h_0}^{\infty} dh\left(1 + \frac{h}{R}\right)^2\left[-\gamma\left(\frac{1}{r_1} - \frac{1}{r_2}\right) + \Pi_N(h)\right] \tag{5}$$

For the equilibrium film thickness $h = h_0$, the expression in the square brackets has to be zero (with precision $\gamma/\mathcal{R}$). The term that includes the capillary pressure of the meniscus is negative and not small in comparison with Π_N. As a result, this term reduces $\cos\theta_N$, and it is exactly what we need to explain the transition to the hydrophobic state. Therefore, we can conclude that the transition to the hydrophobic state can be explained by the formation of the nanomeniscus, when the nanoparticles on the substrate are also wetted.

Comparing the results in Figure 3a,b and Figure 3c,d, after the adsorbing airborne hydrocarbons, the SCA of the amorphous GST NP decorated Cu is higher than the one of the airborne hydrocarbons adsorbed on the *in situ* crystallized GST NPs. The explanation for this difference may stem from two aspects. On one hand, the surface energy of amorphous GST flat surface with adsorbed airborne hydrocarbons (with SCA of 48.5°) is lower than the surface energy of the crystalline one. Therefore, the SCA when airborne hydrocarbons adsorbed on amorphous GST NP decorated Cu surfaces should show higher SCA than the crystalline GST NPs if they share the same morphology. In addition, the coalescence of NPs is stronger for the *in situ* crystallized GST NPs, so the effective radius of the NPs will be larger, and the SCA would be lower when a larger "R" is used in eq 5.

CONCLUSIONS

In summary, the effect of airborne hydrocarbons on the wettability of GST NP decorated surfaces has been extensively studied in a systematic manner. Besides the effect of lowering the surface energy by airborne hydrocarbons, the geometry of the three phase contact area of GST NP decorated surfaces was discussed in order to shed light on the question: Why

DOI: 10.1021/acsnano.9b06909
ACS Nano 2019, 13, 13430−13438

some nanostructured surfaces do not follow the Wenzel model when they show a rose petal type of wettability associated with strong pinning of water droplets. In this respect, our results provide a comprehensive understanding of how strong is the effect of airborne hydrocarbons on the wettability of NP decorated surfaces, indicating that the hydrocarbon adsorption/removal process can effectively manipulate the wettability of nanostructured surfaces. Moreover, our results imply that some previously defined "hydrophilic" materials could be used in a hydrophobic surface design.

METHODS

GST NPs on Cu Blocks. The GST NPs were deposited in a modified *Mantis Nanogen* 50 system on mechanically polished Cu (purity: 99.99%) blocks (area: 1 cm × 1 cm) having a native surface oxide layer. A TEM grid with continuous carbon supporting film was put together with the Cu blocks for subsequent TEM observations. The size and coverage of the GST NPs are controlled by the settings in the *Mantis Nanogen* 50 system. The coverage of NPs was obtained from TEM images. More details can be seen in our previous works.[41,42]

Amorphous GST NPs on Graphene. The 25 μm-thick copper foil (Alfa Aesar, 99.8% purity) was cleaned by soaking in acetic acid for 8 h, rinsed by water, and then put into a quartz tube for graphene growth. The quartz tube was filled with 0.1 mbar hydrogen (Messer, purity 5.0) to eliminate the residual copper oxide on the copper surface. Meanwhile, it was heated up to 1035 °C. Afterward, 0.2 mbar mixture of argon and methane (5%) was added into the quartz tube at 1035 °C for 2 h. Thereafter, the copper foil was cooled down to room temperature with all the gases remaining. Then the graphene was transferred onto Quantifoil R2/1 holey carbon (Electron Microscopy Sciences, Q225-AR1) TEM grids. First, the TEM grids were placed on top of graphene on copper. Two drops of isopropanol (IPA) were deposited on the sample to enhance the bonding between graphene and the carbon membrane of the quantifoil TEM grids after the IPA evaporated. The sample was then annealed at 100 °C for 10 min to finally strengthen the contact between graphene and the TEM grids before the copper was etched away in $(NH_4)_2S_2O_8$ 0.1 g/mL for 24 h. The TEM grids covered with graphene were eventually rinsed three times in demi-water to eliminate any remaining trace of the etchant. Then the graphene covered TEM grids were put as substrate and received GST NPs deposition, the setting for this deposition process is the same as the Cu/GST NPs samples. Therefore, GST NPs were distributed at intervals on graphene and graphene/carbon areas. More details can be seen in our previous work.[43]

TEM Observations. The morphology of the as-deposited NPs was characterized using a JEOL 2010 at 200 kV within 1 h after sample deposition. The energy dispersive spectroscopy elemental maps and high-resolution STEM images were recorded using a JEOL (Accel) ARM 200F (UHR pole piece) equipped with a single 100 mm^2 (0.65 srad) EDX detector and FEI Themis Z equipped with SuperX EDX detectors (four 30 mm^2 detectors providing 0.7 srad). High acceleration voltage (200 kV) was utilized to record overview BF TEM images of the GST NPs, while low acceleration voltages (40 and 60 kV) were used to record STEM images when graphene is involved since high voltage (above 80 kV) can easily induce knock-on damage to the monolayer graphene due to the collision of the beam electrons with the nucleus of the graphene target atom.

Contact Angle Measurement. The contact angle measurements were performed using a Dataphysics OCA25 system. An automated syringe dropped 2 μL droplets of pure water (Milli-Q) on the sample, where a camera recorded the pictures over a period of several seconds. The drop shape is analyzed based on the shape of an ideal sessile drop, the surface curvature of which results only from the force equilibrium between surface tension and weight. The values of the contact angle were obtained *via* a fit using the Young−Laplace (YL) equation based on the shape analysis of a complete drop and also compared to the results obtained from the geometrical CA analysis. For every sample, the CA measurements were repeated for several drops on different sample areas.

GST Films Fabrication. Amorphous and crystalline GST films were deposited on flat silicon with native oxide layer using pulsed laser deposition (PLD) under room temperature and 200 °C, separately. A sintered GST225 powder target from KTECH with 99.999% purity was used, and background pressure was below 10^{-7} mBar. The target was ablated using a KrF excimer laser (248 nm), with a fluence of 1.0 J cm^{-2} and a spot size of 1.3 mm^2. The deposition was performed at room temperature, in 0.12 mbar argon gas with a 1 sccm flow, and a target−substrate distance of 4 cm. The resulting GST films are flat and homogeneous (see Figure S3). The thicknesses of both films are more than 40 nm, which is larger than the cutoff distance of van der Waals interaction between water and GST surfaces and thick enough for evaluation of wettability of GST flat surfaces.

ASSOCIATED CONTENT

Supporting Information

The Supporting Information is available free of charge on the ACS Publications website at DOI: 10.1021/acsnano.9b06909.

Movie 1: The troop of the TPL by injecting water into the meniscus on a GST NP decorated Cu surface to obtain the ACA of the sample (AVI)

Figure S1 schematically shows the hydrocarbon atmosphere created by octane. Figure S2 shows the qualitative behavior of the disjoining pressure for a partially wetting materials. The AFM topology images of the as-prepared GST films are shown in Figure S3 (PDF)

AUTHOR INFORMATION

Corresponding Author

*E-mail: g.palasantzas@rug.nl.

ORCID

Bin Chen: 0000-0003-1591-0843

Vitaly B. Svetovoy: 0000-0002-9649-5663

George Palasantzas: 0000-0002-5084-8769

Notes

The authors declare no competing financial interest.

ACKNOWLEDGMENTS

We would like to acknowledge financial support from the China Scholarship Council (W.G.). Moreover, we would like to acknowledge support from the Zernike Institute for Advanced Materials.

REFERENCES

(1) Jiang, L.; Zhao, Y.; Zhai, J. A Lotus-Leaf-Like Superhydrophobic Surface: A Porous Microsphere/Nanofiber Composite Film Prepared by Electrohydrodynamics. *Angew. Chem.* **2004**, *116*, 4438−4441.

(2) Marmur, A. The Lotus Effect: Superhydrophobicity and Metastability. *Langmuir* **2004**, *20*, 3517−3519.

(3) Patankar, N. A. Mimicking the Lotus Effect: Influence of Double Roughness Structures and Slender Pillars. *Langmuir* **2004**, *20*, 8209−8213.

(4) Feng, L.; Zhang, Y.; Xi, J.; Zhu, Y.; Wang, N.; Xia, F.; Jiang, L. Petal Effect: A Superhydrophobic State with High Adhesive Force. *Langmuir* **2008**, *24*, 4114−4119.

(5) Blossey, R. Self-Cleaning Surfaces — Virtual Realities. *Nat. Mater.* **2003**, *2*, 301−306.

(6) Cao, L.; Jones, A. K.; Sikka, V. K.; Wu, J.; Gao, D. Anti-Icing Superhydrophobic Coatings. *Langmuir* **2009**, *25*, 12444−12448.

DOI: 10.1021/acsnano.9b06909
ACS Nano 2019, 13, 13430−13438

(7) Jhee, S.; Lee, K.-S.; Kim, W.-S. Effect of Surface Treatments on the Frosting/Defrosting Behavior of a Fin-Tube Heat Exchanger. *Int. J. Refrig.* **2002**, *25*, 1047−1053.
(8) Azad, M. a. K.; Ellerbrok, D.; Barthlott, W.; Koch, K. Fog Collecting Biomimetic Surfaces: Influence of Microstructure and Wettability. *Bioinspiration Biomimetics.* **2015**, *10*, No. 016004.
(9) Young, T., III An Essay on the Cohesion of Fluids. *Philos. Trans. R. Soc. London* **1805**, *95*, 65−87.
(10) Wenzel, R. N. Resistance of Solid Surfaces to Wetting by Water. *Ind. Eng. Chem.* **1936**, *28*, 988.
(11) Cassie, A. B. D.; Baxter, S. Wettability of Porous Surfaces. *Trans. Faraday Soc.* **1944**, *40*, 546−551.
(12) Pease, D. C. The Significance of the Contact Angle in Relation to the Solid Surface. *J. Phys. Chem.* **1945**, *49*, 107−110.
(13) Gao, L.; McCarthy, T. J. How Wenzel and Cassie Were Wrong. *Langmuir* **2007**, *23*, 3762−3765.
(14) Gao, L.; McCarthy, T. J. Contact Angle Hysteresis Explained. *Langmuir* **2006**, *22*, 6234−6237.
(15) Dupré, A.; Dupré, P. In *Théorie Mécanique de la Chaleur*; Gauthier-Villars: Paris, 1869.
(16) Extrand, C. W. Contact Angles and Hysteresis on Surfaces with Chemically Heterogeneous Islands. *Langmuir* **2003**, *19*, 3793−3796.
(17) Wang, L.; Zhao, Y.; Tian, Y.; Jiang, L. A General Strategy for the Separation of Immiscible Organic Liquids by Manipulating the Surface Tensions of Nanofibrous Membranes. *Angew. Chem., Int. Ed.* **2015**, *54*, 14732−14737.
(18) Derjaguin, B. V. Theory of Capillary Condensation and Other Capillary Phenomena Accounting for the Disjoining Pressure of Polymolecular Liquid Films. *Acta Physicochim. URSS* **1940**, *12*, 181−200.
(19) Derjaguin, B. V.; Churaev, N. V.; Muller, V. M. In *Surfaces Forces*; Consultant Bureau: New York and London, 1987.
(20) Bernett, M. K.; Zisman, W. A. Confirmation of Spontaneous Spreading by Water on Pure Gold. *J. Phys. Chem.* **1970**, *74*, 2309−2312.
(21) Li, Z.; Wang, Y.; Kozbial, A.; Shenoy, G.; Zhou, F.; McGinley, R.; Ireland, P.; Morganstein, B.; Kunkel, A.; Surwade, S. P.; Li, L.; Liu, H. Effect of Airborne Contaminants on the Wettability of Supported Graphene and Graphite. *Nat. Mater.* **2013**, *12*, 925−931.
(22) Zubkov, T.; Stahl, D.; Thompson, T. L.; Panayotov, D.; Diwald, O.; Yates, J. T. Ultraviolet Light-Induced Hydrophilicity Effect on TiO2(110)(1 × 1). Dominant Role of the Photooxidation of Adsorbed Hydrocarbons Causing Wetting by Water Droplets. *J. Phys. Chem. B* **2005**, *109*, 15454−15462.
(23) Boinovich, L. B.; Emelyanenko, A. M.; Pashinin, A. S.; Lee, C. H.; Drelich, J.; Yap, Y. K. Origins of Thermodynamically Stable Superhydrophobicity of Boron Nitride Nanotubes Coatings. *Langmuir* **2012**, *28*, 1206−1216.
(24) Wang, J.; Liu, J.; Neate, N.; Bai, M.; Xu, F.; Hussain, T.; Scotchford, C.; Hou, X. Investigation on Time-Dependent Wetting Behavior of Ni-Cu-P Ternary Coating. *J. Alloys Compd.* **2018**, *765*, 221−228.
(25) Choi, K.; Eom, T.-J.; Lee, C. Comparison of the Removal Efficiency for Organic Contaminants on Silicon Wafers Stored in Plastic Boxes between UV/O3 and ECR Oxygen Plasma Cleaning Methods. *Thin Solid Films* **2003**, *435*, 227−231.
(26) Lu, Y.; Sathasivam, S.; Song, J.; Crick, C. R.; Carmalt, C. J.; Parkin, I. P. Robust Self-Cleaning Surfaces That Function When Exposed to Either Air or Oil. *Science* **2015**, *347*, 1132−1135.
(27) ten Brink, G. H.; Foley, N.; Zwaan, D.; Kooi, B. J.; Palasantzas, G. Roughness Controlled Superhydrophobicity on Single Nanometer Length Scale with Metal Nanoparticles. *RSC Adv.* **2015**, *5*, 28696−28702.
(28) Meinders, E. R.; Mijiritskii, A. V.; Pieterson, L. van; Wuttig, M. In *Optical Data Storage: Phase-Change Media and Recording*; Springer Science & Business Media: Berlin, 2006.
(29) Wuttig, M.; Yamada, N. Phase-Change Materials for Rewriteable Data Storage. *Nat. Mater.* **2007**, *6*, 824−832.
(30) Garaj, S.; Hubbard, W.; Reina, A.; Kong, J.; Branton, D.; Golovchenko, J. A. Graphene as a Subnanometre Trans-Electrode Membrane. *Nature* **2010**, *467*, 190−193.
(31) Zhu, Y.; Murali, S.; Stoller, M. D.; Ganesh, K. J.; Cai, W.; Ferreira, P. J.; Pirkle, A.; Wallace, R. M.; Cychosz, K. A.; Thommes, M.; Su, D.; Stach, E. A.; Ruoff, R. S. Carbon-Based Supercapacitors Produced by Activation of Graphene. *Science* **2011**, *332*, 1537−1541.
(32) O'Hern, S. C.; Stewart, C. A.; Boutilier, M. S. H.; Idrobo, J.-C.; Bhaviripudi, S.; Das, S. K.; Kong, J.; Laoui, T.; Atieh, M.; Karnik, R. Selective Molecular Transport through Intrinsic Defects in a Single Layer of CVD Graphene. *ACS Nano* **2012**, *6*, 10130−10138.
(33) Kim, K.-S.; Lee, H.-J.; Lee, C.; Lee, S.-K.; Jang, H.; Ahn, J.-H.; Kim, J.-H.; Lee, H.-J. Chemical Vapor Deposition-Grown Graphene: The Thinnest Solid Lubricant. *ACS Nano* **2011**, *5*, 5107−5114.
(34) Lee, C.; Wei, X.; Kysar, J. W.; Hone, J. Measurement of the Elastic Properties and Intrinsic Strength of Monolayer Graphene. *Science* **2008**, *321*, 385−388.
(35) Chen, B.; ten Brink, G. H.; Palasantzas, G.; Kooi, B. J. Size-Dependent and Tunable Crystallization of GeSbTe Phase-Change Nanoparticles. *Sci. Rep.* **2016**, *6*, 39546.
(36) ten Brink, G. H.; van het Hof, P. J.; Chen, B.; Sedighi, M.; Kooi, B. J.; Palasantzas, G. Control Surface Wettability with Nanoparticles from Phase-Change Materials. *Appl. Phys. Lett.* **2016**, *109*, 234102.
(37) Bowen, W. R.; Doneva, T. A. In *Encyclopedia of Surface and Colloid Science*; Hubbard, A. T., Ed.; Marcel Dekker Inc.: New York, 2002.
(38) Frumkin, A. N. On Wetting and Sticking Phenomena. *Zhurn. Phys. Chem. (USSR)* **1938**, *12*, 337−345.
(39) Churaev, N. V. Contact Angles and Surface Forces. *Adv. Colloid Interface Sci.* **1995**, *58*, 87−118.
(40) Boinovich, L.; Emelyanenko, A. The Prediction of Wettability of Curved Surfaces on the Basis of the Isotherms of the Disjoining Pressure. *Colloids Surf., A* **2011**, *383*, 10−16.
(41) ten Brink, G. H.; Krishnan, G.; Kooi, B. J.; Palasantzas, G. Copper Nanoparticle Formation in a Reducing Gas Environment. *J. Appl. Phys.* **2014**, *116*, 104302.
(42) Chen, B.; ten Brink, G. H.; Palasantzas, G.; Kooi, B. J. Crystallization Kinetics of GeSbTe Phase-Change Nanoparticles Resolved by Ultrafast Calorimetry. *J. Phys. Chem. C* **2017**, *121*, 8569−8578.
(43) Chen, B.; Do, V. L.; ten Brink, G.; Palasantzas, G.; Rudolf, P.; Kooi, B. J Dynamics of GeSbTe Phase-Change Nanoparticles Deposited on Graphene. *Nanotechnology* **2018**, *29*, 505706.

DOI: 10.1021/acsnano.9b06909
ACS Nano 2019, 13, 13430−13438